

Wing Morphology and Inertial Properties of Bumblebees

Dmitry Kolomenskiy^{a,*}, Sridhar Ravi^b, Ru Xu^{c,d}, Kohei Ueyama^c, Timothy Jakobi^b,
Thomas Engels^{e,f}, Toshiyuki Nakata^c, Jörn Sesterhenn^f, Marie Farge^e,
Kai Schneider^g, Ryo Onishi^a, and Hao Liu^c

^a JAMSTEC, Japan

^b University of New South Wales at the Australian Defence Force Academy, Australia

^c Chiba University, Japan

^d Shanghai Jiao Tong University, China

^e ENS Paris, France

^f TU Berlin, Germany

^g I2M, CNRS & Aix-Marseille University, France

Abstract—It is shown that the wings of bumblebees during flapping undergo pitching (feathering angle) rotation that can be characterized as a fluid-structure interaction problem. Measurements of shape, size and inertial properties of the wings of bumblebees *Bombus ignitus* are described that provide the necessary input data for numerical modelling. A computational fluid dynamics (CFD) solver is combined with a dynamical model that describes the time evolution of the feathering angle. An example result of the numerical simulation is shown.

Index Terms—Flapping flight, insect, bumblebee, wing, moment of inertia, fluid-structure interaction.

I. INTRODUCTION

Flapping wings of insects are designed such that they produce positive lift during both upstroke and downstroke. This is achieved by large pitching (feathering angle) rotations at the end of each half-cycle necessary for maintaining positive kinematic angle of attack. Computations and experiments with robotic flappers (e.g., [1,2]) have demonstrated that similar kinematic patterns can be produced by a wing with only up- and downstroke motion being prescribed, and elastic hinge attachment permitting passive pitching rotation. By construction, this model mimics dipteran wings. However, it may be suitable for hymenopterans as well since their hindwings are connected to the forewings by hooks. To assess the accuracy of this hypothesis for bumblebees is the ultimate goal of our study. We use experiments and numerical simulations to achieve it, and one of the critical steps is to collect reliable input data for the numerical modelling. This paper aims to provide a detailed account of the procedure that we have followed to determine the geometrical and inertial properties of the bumblebee wings. Although there have been previous studies describing the wing mass

distribution in flies [3], dragonflies [4] and beetles [5], to the best of our knowledge, there have been no such measurement reported for bumblebees. The novelty of our work resides not only in the choice of the target species, but also in the measurement method that differentiates between the vein mass and the membrane mass. Finally, the paper provides an outlook on the serviceableness of these measurements by showing an example numerical modelling result in comparison with flight experiment data.

II. METHODS

A. Study Specimens

Bumblebees (*Bombus ignitus*) from a commercial breeder (Mini Polblack, Koppert, Arysta LifeScience Asia, Japan) were maintained in laboratory conditions. The hives were part of the flight experiment facility described in a greater detail in [6]. Individual bees were randomly selected for the measurements reported in the following sections.

B. Numerical Bumblebee Model

We model the fluid-structure interaction of the flapping wings using *FluSI*, a pseudo-spectral Navier-Stokes solver with volume penalization [7]. For the purposes of this study, the solver has been modified to include the wing motion model based on the time evolution of the feathering angle according to the following driven oscillator equation [1]:

$$\begin{aligned} J_{xx}\ddot{\alpha} &= M_{aero} - K(\alpha - \alpha_0) - C\dot{\alpha} + \\ J_{xx} \left[\frac{1}{2}(\dot{\phi}^2 \cos^2 \theta - \theta^2) \sin 2\alpha - \ddot{\phi} \sin \theta - \right. \\ &\left. \dot{\phi} \dot{\theta} \cos \theta (1 + \cos 2\alpha) \right] + J_{xy} \left[\ddot{\phi} \cos \theta \cos \alpha + \right. \\ &\left. \ddot{\theta} \sin \alpha + \frac{1}{2} \dot{\phi}^2 \sin 2\theta \sin \alpha - 2\dot{\phi} \dot{\theta} \sin \theta \cos \alpha \right], \end{aligned}$$

* Corresponding author: 3173-25 Showa-machi, Kanazawa-ku, Yokohama Kanagawa, 236-0001, Japan, E-mail: dkolom@gmail.com

where the wing positional angle ϕ and elevation angle θ are prescribed as time-periodic functions on the basis of the data collected in flight experiments [6], and the feathering angle α is calculated using numerical integration. J_{xx} is the moment of inertia with respect to the pitching (feathering) axis and J_{xy} is the only non-zero off-diagonal term of the moment of inertia tensor of the wing, since it is modelled as a thin flat plate. The aerodynamic pitching moment M_{aero} is obtained by integrating the fluid forces acting on the wing. The shoulder hinge joint is modelled as a torsional spring with stiffness K , damping coefficient C and neutral angle α_0 , which are *a priori* unknown. An optimization study to determine their possible values will be described in full length elsewhere [8]. Let us focus in the next sections of this paper on measuring the shape and the inertial properties of the wings. They constitute prerequisite input data for the numerical simulations.

C. Wing Mass Measurement

Statistical data of the bumblebee wing mass were collected for $n=13$ individuals. Workers and queens were used for this purpose, as they have similar wing structure but differ in size. The bees were cold-anaesthetized in a refrigerator at 3°C, the wings were cut off and immediately used for the mass measurements. Each set of two forewings and two hindwings was weighed three times on a microbalance (AUW220D, Shimadzu, Japan). The average of each three measurements, divided by two, was taken as the measured value of the wing mass m_w , that we define as the mass of one forewing and one hindwing, $m_w = m_f + m_h$, assuming that the left and the right wings are of the same mass. The wing length R was measured with a digital caliper. Since all wings were cut at slightly different locations, the measured values of R and m_w were corrected using linear extrapolation in proportion to the full length of each wing from the shoulder hinge joint to the wing tip. The full length was calculated as a sum of the measured length and the length of the discarded part. The latter was estimated using the venation pattern near the shoulder, assumed to be geometrically similar for all wings.

D. Wing Contour Measurement

The input data required for numerical simulation of passive feathering rotations includes wing shape and moments of inertia. In our model, we approximate the wings as flat plates and only account for the wing planar shape. Deviation from the planar shape may have important consequences for the force generation but, to account for it properly, wing deformation should be taken into consideration, which is beyond the scope of this work.

To obtain the wing outlines, wings were glued on millimeter paper and photographic images were taken. 20 forewings and 18 hindwings were used. To distinguish the wing from the background, a threshold of gray value for binarization was obtained by trial and error using a custom software written in *Matlab*

(MathWorks, USA). Figure 1 shows an example. All wings were aligned along their major axes before edge detection. All wing outlines were rescaled by their maximum wing chord length, then aligned to obtain the best match in leading edge. The forewings and the hindwings were treated separately.

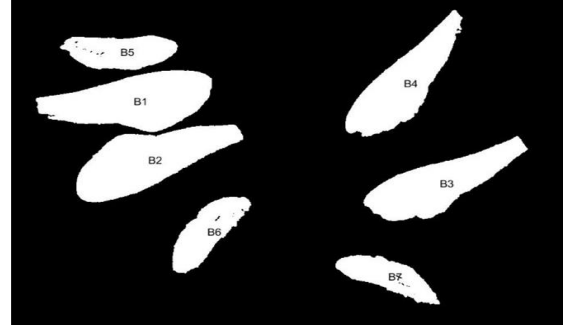


Fig. 1 Wing image after choosing threshold of gray value for binarization.

The average wing contour calculation can be simplified through a transform from Cartesian coordinates to polar coordinates, since averaging is conducted towards a single valued function in polar coordinates instead of multivalued function in Cartesian coordinates then. Thus, the origin of the polar coordinate system is selected at a fixed offset from the wing root (at 70% in the spanwise direction and 50% between the front point of the leading edge and the rear point of the trailing edge). Then, the polar radius is calculated for a set of 150 values of the polar angle uniformly distributed between 0 and 2π . The mean and the standard deviation (STD) are then calculated for each point of the wing contour by using all of the wing samples. Finally, the mean contour is transformed into the Cartesian coordinates, as well as the contours that correspond to the mean polar radius ± 1 and ± 2 STD, see Fig. 2.

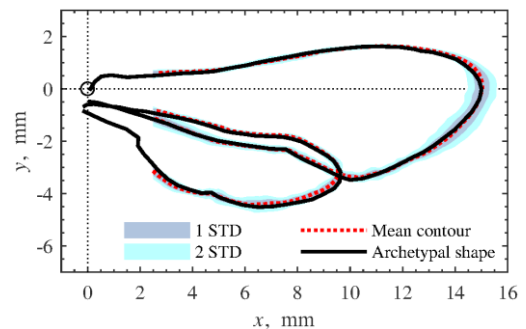


Fig. 2 The shape variation of bumblebee wings.

E. Vein Morphology Measurement

In addition to the statistical analysis, one image was digitized manually using *Engauge Digitizer* software [9], for the purpose of obtaining the wing contours for the CFD model and vein coordinates for the mass distribution model. The vein thickness, necessary for estimating the mass distribution, could not be reliably determined from photographic images. We measured the vein thickness from micro-CT scans (inspeXio SMX-100CT, Shimadzu, Japan) with 0.037 mm voxel resolution. A forewing and a hindwing separately were glued on stainless steel pins at their roots and were stored

refrigerated for about two hours prior to measurement. Example images from the CT-scan are shown in Fig. 3. The left part of the figure shows the front view of each piece of the wing, and the right part of the figure shows several horizontally oriented planar sections (i.e., sections perpendicular to the pin). The wing is not flat, therefore, the example planar sections shown in the figure are not exactly perpendicular to the wing. But the deviation from perpendicularity is less than 30 degrees so that the wing thickness can be determined from these images with less than 15% error, which is of the same order of magnitude as the spatial resolution of the CT scan. In some particular cases we also examined planes oriented perpendicularly to selected veins.

Based on the CT scan data, we classified the veins and measured the thickness of each vein near its middle point using *myVGL* viewer (Volume Graphics, Germany). Several measurements in different directions were acquired to determine the nominal circular-cylinder diameter of the vein d_v and its uncertainty interval δ_v defined as the half-difference between the maximum and the minimum data point values in the measurement. Since the CT-scanned wing was larger than the photographed wing used for measuring the venation pattern ($R=17$ mm vs 15 mm, respectively), the vein diameters were downscaled isometrically.

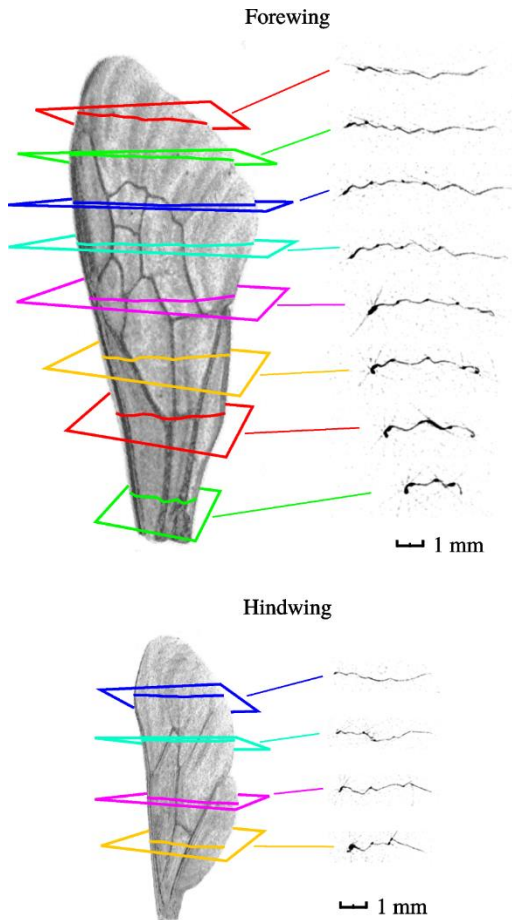


Fig. 3 Example micro-CT images of a forewing and a hindwing of the same individual with $R=17$ mm. Planar cross-sections correspond to the stations schematically shown using color annotations.

F. Estimation of Moments of Inertia

The moments of inertia are calculated as sums of contributions from the membrane and the veins, i.e.

$$J_{xx} = J_{mxx} + J_{vxx}, \quad J_{yy} = J_{myy} + J_{vyy},$$

$$J_{xy} = J_{mxy} + J_{vxy},$$

which is possible due to linearity of the inertia tensor with respect to the material density. The veins are discriminated from the membrane using the morphological model described above. The moments of inertia of the veins are calculated using the measured length and diameter of the veins,

$$J_{vxx} = \int_{\Gamma_{vf}} \frac{1}{4}\pi\rho_c y_v^2 d_v^2 dl_v + \int_{\Gamma_{vh}} \frac{1}{4}\pi\rho_c y_v^2 d_v^2 dl_v$$

$$J_{vyy} = \int_{\Gamma_{vf}} \frac{1}{4}\pi\rho_c x_v^2 d_v^2 dl_v + \int_{\Gamma_{vh}} \frac{1}{4}\pi\rho_c x_v^2 d_v^2 dl_v$$

$$J_{vxy} = \int_{\Gamma_{vf}} \frac{1}{4}\pi\rho_c x_v y_v d_v^2 dl_v + \int_{\Gamma_{vh}} \frac{1}{4}\pi\rho_c x_v y_v d_v^2 dl_v$$

where dl_v is the elementary length of small linear elements of the veins that belong to the forewing (Γ_{vf}) or to the hindwing (Γ_{vh}), respectively. Material density of the veins equal to that of the cuticle, $\rho_c = 1300$ kg/m³ [10], is assumed. The integrals are evaluated numerically by discretizing the veins using line elements of small length, then summing up the masses of all elements.

Contribution from the membrane is calculated as

$$J_{mxx} = \int_{\Sigma_{mf}} y_w^2 \rho_f dx_w dy_w + \int_{\Sigma_{mh}} y_w^2 \rho_h dx_w dy_w$$

$$J_{myy} = \int_{\Sigma_{mf}} x_w^2 \rho_f dx_w dy_w + \int_{\Sigma_{mh}} x_w^2 \rho_h dx_w dy_w$$

$$J_{mxy} = \int_{\Sigma_{mf}} x_w y_w \rho_f dx_w dy_w + \int_{\Sigma_{mh}} x_w y_w \rho_h dx_w dy_w$$

where surface integration is performed over the forewing membrane (Σ_{mf}) and the hindwing membrane (Σ_{mh}) placed in the coordinate system of the wing in its flight position, which corresponds to the wing shape in Fig. 2. For the hindwing, we assume uniform area density of the membrane, $\rho_h = \rho_{h0} = (m_h - m_{vh})/A_h$, where A_h is the hindwing area. This fully defines the mass distribution over the surface of the hindwing. However, the area density of the forewing membrane is far from being uniform, and we approximate its distribution with a bilinear function $\rho_f = \rho_{f0} + x\rho_{fx} + y\rho_{fy}$, where the coefficients ρ_{f0} , ρ_{fx} and ρ_{fy} are determined using optimization, with the wing mass as a constraint. As a target function for minimization, we choose the r.m.s. deviation from a measured coarse-grain mass distribution. In a separate measurement ($n=3$ samples), we cut wings in segments and weighed each segment. On the other hand, the segment mass can be calculated as an integral of the bilinear approximation ρ_f over the segment area, plus the vein mass of the same segment. Thus, we define the target function as the r.m.s. deviation between the measured and the calculated segment mass per unit area. Its minimization provides the optimal values of the coefficients ρ_{fx} and ρ_{fy} to be used in the bilinear fit when calculating the moments of inertia.

Note that, in [3,4,5], the area density distribution was determined as the dissected wing segment mass divided by the respective area. Our approach of calculating separately the vein mass and the membrane mass is less straightforward, but it allows us to use only a small number of segments and still account for the important area density variation near the leading edges and the roots, because it is mainly due to the veins.

Once the mass distribution is determined, it is useful to calculate the position of the wing center of mass, even though this quantity does not enter in the wing rotation model. The center of mass is determined using formulae $x_c = (S_{vy} + S_{my})/m_w$ and $y_c = (S_{vx} + S_{mx})/m_w$, where

$$\begin{aligned} S_{vx} &= \int_{\Gamma_{vf}} \frac{1}{4}\pi\rho_c y_v d_v^2 dl_v + \int_{\Gamma_{vh}} \frac{1}{4}\pi\rho_c y_v d_v^2 dl_v, \\ S_{vy} &= \int_{\Gamma_{vf}} \frac{1}{4}\pi\rho_c x_v d_v^2 dl_v + \int_{\Gamma_{vh}} \frac{1}{4}\pi\rho_c x_v d_v^2 dl_v, \\ S_{mx} &= \int_{\Sigma_{mf}} y_w \rho_f dx_w dy_w + \int_{\Sigma_{mh}} y_w \rho_h dx_w dy_w, \\ S_{my} &= \int_{\Sigma_{mf}} x_w \rho_f dx_w dy_w + \int_{\Sigma_{mh}} x_w \rho_h dx_w dy_w. \end{aligned}$$

III. RESULTS AND DISCUSSION

A. Wing Morphology

The dotted lines in Fig. 2 show the mean contours of the forewing and the hindwing. The area filled with grey color displays the interval of ± 1 STD, calculated in polar coordinates. Light blue color shows the ± 2 STD interval. The archetypal wing contour used in the CFD simulations is shown in Fig. 2 with a solid black line. Most of its part lies within the ± 1 STD band, and it lies entirely in the ± 2 STD band. Visually, it is only slightly different from the mean contour obtained by statistical averaging over all samples. Note that the sample that we selected for the wing contour in the CFD simulations was that of an intact wing, while some of the samples used for the statistical averaging showed considerable wear. The mean chord length, defined as the wing area divided by R , is equal to $c = 0.273R$.

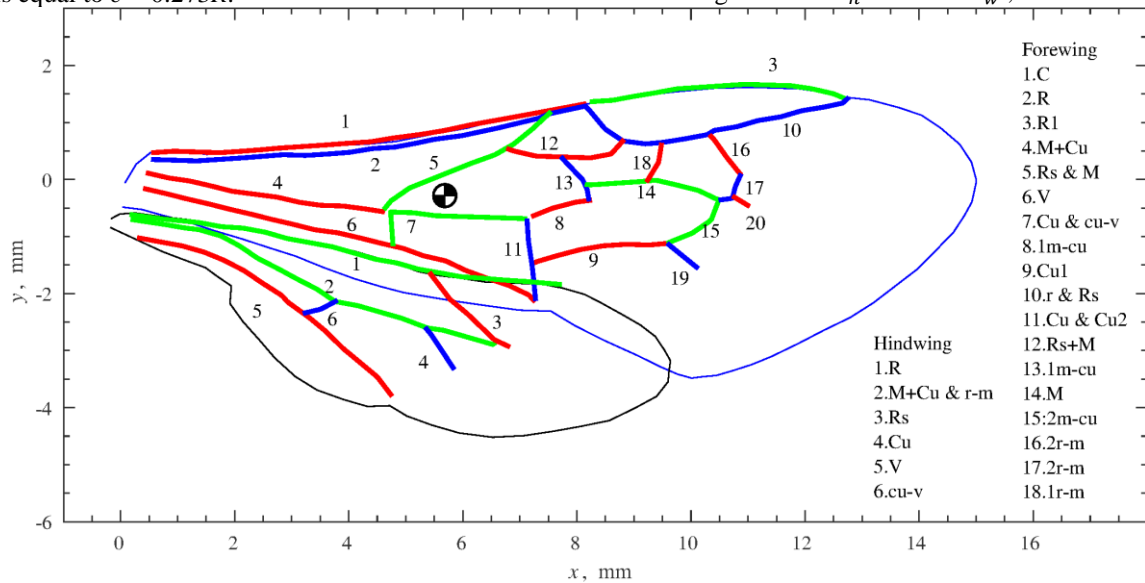


Fig. 5 Vein number and the corresponding position in forewing and hindwing. The black and white marker shows the center of mass. The wing length is equal to $R = 15$ mm in this example.

B. Wing Mass and Moments of Inertia

The measured wing mass data points are shown in Fig. 4 as blue circles. The average wing length is 15.38 mm and the average wing mass is equal to 0.836 mg. The red dashed curve shows a regression line calculated using linear regression of $\log(m_w)$ as a function of $\log(R)$. This power law $m_w \sim R^{3.04}$ is remarkably close to the isometric scaling $m_w \sim R^3$ that holds for geometrically similar wings. We therefore use the isometric scaling in our subsequent analysis.

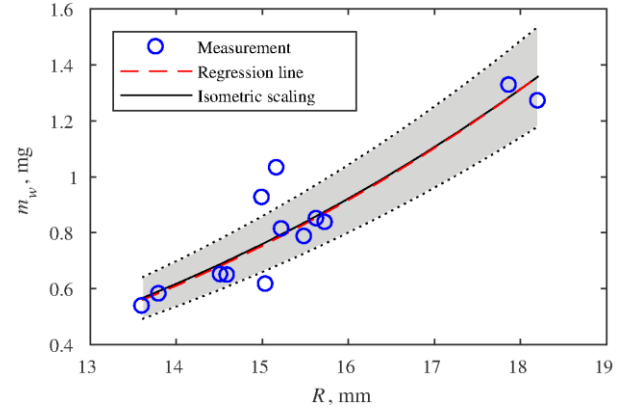


Fig. 4 Wing mass (one forewing plus one hindwing) as a function of the wing length.

We calculated the mean m_w/R^3 and its standard deviation for all measurement data points, and obtained the scaling law $m_w = (0.2251 \pm 0.0296)R^3$, where R is in meters and m_w is in kilograms. The mean $m_w(R)$ is shown in Fig. 4 with a black solid line, and the ± 1 STD interval is shown as a gray-filled band. For a wing of length $R = 15.2$ mm in our example numerical simulation, the mass is equal to 0.791 mg. Relative mass of forewings and hindwings was determined from separate measurements using $n=4$ samples. The results show that forewing mass is $m_f = 0.806m_w$ and the hindwing mass is $m_h = 0.194m_w$, on the average.

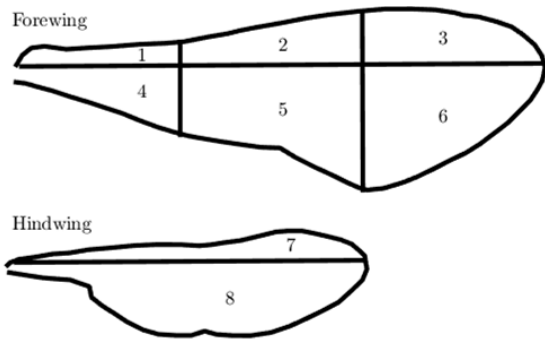


Fig. 6 Segmentation of the wing for mass distribution measurement.

The planar location of the veins obtained from a photographic image is shown in Fig. 5. Different color segments marked with different numbers each have approximately constant thickness, and the measured values are displayed in Table 1, which shows the nominal values of the vein diameters, normalized by R , and the corresponding uncertainty intervals. Using these geometrical parameters and uniform vein density, we find that the relative contribution of veins to the forewing mass is equal to $m_{vf}/m_f = 0.61$. For the hindwing veins, it is equal to $m_{vh}/m_h = 0.90$. The membrane contributes to the remaining 39% of the forewing mass and 10% of the hindwing mass.

Table 1 Vein non-dimensional thickness d_v/R and measurement uncertainty interval δ_v/R .

Forewing			Hindwing		
#	Nominal thickness	Uncertainty interval	#	Nominal thickness	Uncertainty interval
1	0.0070	0.0011	1	0.0065	0.0005
2	0.0074	0.0009	2	0.0043	0.0004
3	0.0055	0.0004	3	0.0046	0.0006
4	0.0051	0.0011	4	0.0011	0.0008
5	0.0040	0.0007	5	0.0038	0.0006
6	0.0048	0.0010	6	0.0037	0.0006
7	0.0040	0.0010			
8	0.0038	0.0010			
9	0.0041	0.0010			
10	0.0048	0.0008			
11	0.0045	0.0012			
12	0.0038	0.0010			
13	0.0042	0.0011			
14	0.0038	0.0009			
15	0.0034	0.0008			
16	0.0032	0.0012			
17	0.0032	0.0010			
18	0.0044	0.0015			
19	0.0015	0.0014			
20	0.0018	0.0017			

Segmentation of the wing used for the linear regression analysis of the membrane density distribution is shown in Fig. 6. Every segment is labelled with a number. The area density of each segment can be determined from Table 2. The values in the table correspond to the wing segment mass, divided by the area of the same segment and by the wing length R . The values obtained directly from mass measurements are

shown in the second last column. Note that they include both the membrane and the vein. This coarse segmentation is sufficient for evaluation of the bi-linear and uniform models of membrane density of the forewing and the hindwing, respectively. The optimal linear regression approximation parameters of the membrane are as follows: $\rho_{f0}/R = 0.826 \text{ kg/m}^3$, $\rho_{fx} = -0.798 \text{ kg/m}^3$, $\rho_{fy} = 0.672 \text{ kg/m}^3$, $\rho_{h0}/R = 0.045 \text{ kg/m}^3$. Integration of this membrane density distribution and summation with the vein mass leads to the values in the last column. The agreement between the values in the two columns speaks in support of the regression model.

Calculation of the moments of inertia yields the following isometric scaling relationships:

$$J_{xx} = 0.0014R^5, \quad J_{yy} = 0.0426R^5, \\ J_{xy} = -0.0010R^5,$$

where R is in meters and the result is in $\text{kg} \cdot \text{m}^2$. For a wing of length $R = 15.2 \text{ mm}$, we obtain $J_{xx} = 1.14 \cdot 10^{-12} \text{ kg} \cdot \text{m}^2$, $J_{yy} = 34.6 \cdot 10^{-12} \text{ kg} \cdot \text{m}^2$, $J_{xy} = -0.81 \cdot 10^{-12} \text{ kg} \cdot \text{m}^2$.

In order to estimate the error in the inertia calculation induced when the veins are approximated as circular cylinders, we repeated the inertia calculations 33 times with the thickness of each vein modified as $d_v + \chi \delta_v$, where the values of χ were taken randomly between -1 and 1 with uniform probability distribution. We thus obtained sequences of values for each component of the inertia tensor. They have the mean values equal up to the last digit to the nominal values shown above, and the standard deviations equal to $\Delta J_{xx} = 0.00006R^5$, $\Delta J_{yy} = 0.00140R^5$, $\Delta J_{xy} = 0.00023R^5$, respectively.

The full wing center of mass is located remarkably near to the rotation axis at $x_c = 0.379R$, $y_c = -0.019R$. This result, based on calculation as described above, turns out to be close to our quick first estimate obtained by placing clipped wings on a prism: $x_c = 0.42R$, $y_c = -0.03R$.

Table 2 Area density of the wing segments divided by the wing length R , in kg/m^3 .

	Segment	Measured(mean±STD)	Calculated
Fore wing	1	3.64 ± 0.44	3.52
	2	1.66 ± 0.07	1.90
	3	0.87 ± 0.10	0.60
	4	1.48 ± 0.08	1.22
	5	0.49 ± 0.03	0.65
	6	0.16 ± 0.001	0.17
Hind wing	7	1.38 ± 0.13	1.28
	8	0.24 ± 0.04	0.27

Sometimes, the wing is approximated as an ellipse with uniform density in order to simplify the calculation of its moments of inertia. The hinge point is offset from the centroid by a distance a in the spanwise direction towards the wing root and by $b/2$ in the chordwise direction towards the leading edge, where a and b are the major and the minor semi-axes, respectively. In that approximation, the area density is equal to $\rho_w^{ell} = m_w/\pi ab$. The moments of inertia with respect to the hinge point are calculated using the parallel axis

theorem, that yields $J_{xx}^{ell} = \rho_w^{ell}(\pi ab(b/2)^2 + \pi ab^3/4)$, $J_{yy}^{ell} = \rho_w^{ell}(\pi ab a^2 + \pi a^3 b/4)$, $J_{xy}^{ell} = -\rho_w^{ell}\pi ab ab/2$. After substituting $a = R/2$, $b = 2c/\pi$, using the previously determined scaling $c = 0.273R$ for the mean chord and $m_w = 0.2251R^3$ for the wing mass, we obtain $J_{xx}^{ell} = 0.0034R^5$, $J_{yy}^{ell} = 0.0703R^5$, $J_{xy}^{ell} = -0.0098R^5$. We thus find that, for the ellipse model, the xx and yy components differ by a factor of 2 from the morphology-based estimates, and the xy component is one order of magnitude greater. The main reason for this inaccuracy of the ellipse model is that it allocates too much mass near the trailing edge. We therefore stick to the morphology-based relations for J_{xx} , J_{yy} and J_{xy} given earlier in this section.

C. Wing pitching motion

Let us consider an example result of a numerical simulation, which is shown in Fig. 7. It corresponds to hovering flight of a bumblebee with the following parameters: body mass $m_b = 418$ mg, wing length $R = 15.2$ mm, flapping frequency $f = 136$ Hz, wing beat amplitude $\Phi = 137$ deg, body angle $\beta = 41$ deg, anatomical stroke plane angle $\eta = 53$ deg. The elastic hinge model is used with the following parameters: stiffness $K = 2.61 \cdot 10^{-6}$ N·m, damping $C = 0$, neutral angle $\alpha_0 = -1.4$ deg. Periodic symmetric time profiles of the wing angles $\phi(t)$, $\theta(t)$ and $\alpha(t)$, shown with black dash, dash-dot and solid lines, respectively, are derived from flight experiment measurement.

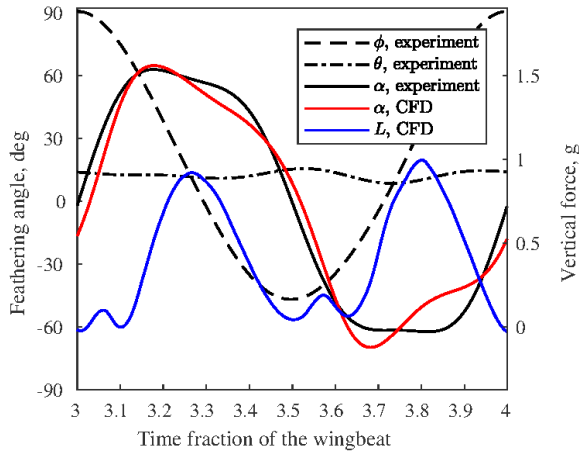


Fig. 7 Time evolution of the wing angles and the vertical aerodynamic force. Note that ϕ and θ in the CFD are identical with the experimental values.

The red line shows the time evolution of α obtained from the CFD model with the same $\phi(t)$, $\theta(t)$. The r.m.s. distance between the time evolution of α in the experiment and during the 4th wingbeat cycle of the numerical simulation is less than 9 deg. The two profiles have essentially the same shape. The most prominent difference is during upstroke where the CFD profile shows a narrower minimum. It can be explained by substantial rotation of the hindwing relative to the forewing that is not accounted for in the model. Since the passive rotation model is in a reasonable agreement with the experiment in terms of $\alpha(t)$, it is not surprising that the time-varying vertical force $L(t)$ obtained from the

model (blue line) displays the double peak profile typical of hovering insects, and that the mean vertical force is equal to 407 mgf, which is within 3% of the measured body mass.

IV. CONCLUSIONS

Morphological measurements of the wings of bumblebees *B. ignitus* are described. It is found that the isometric scaling relation adequately describes the variation of the wing mass with the wing length. An archetypical wing shape and the surface density distribution are derived and used for evaluation of the moments of inertia. Using these geometrical and inertial properties as input data for a numerical simulation that implements the passive feathering rotation model, we observe that the wing rotation about its feathering axis during hovering flight can be adequately described from the standpoint of fluid-structure interaction, as hypothesized in the introduction. Thus, the selected example simulation result differs from the experiment by less than 9 deg in terms of the r.m.s. error in $\alpha(t)$.

V. ACKNOWLEDGEMENTS

DK gratefully acknowledges financial support from the JSPS Grant-in-Aid JP18K13693, thanks Shimadzu Corp. for granting access to the CT system, and Dr. Hiroto Tanaka for his advice and assistance with mass measurements. TE, JS, MF, KS gratefully acknowledge financial support from the Agence nationale de la recherche (ANR Grant 15-CE40-0019) and Deutsche Forschungsgemeinschaft (DFG Grant SE 824/26-1), project AIFIT, and financial support granted by the Ministère de l'Europe et des affaires étrangères (MEAE), Ministère de l'enseignement supérieur, de la recherche et de l'innovation (MESRI), and the Deutscher Akademischer Austauschdienst (DAAD) within the French-German Procope project FIFIT. This work was granted access to the HPC resources of IDRIS (Institut du Développement et des Ressources en Informatique Scientifique) under the allocation made by GENCI (Grand Équipement National de Calcul Intensif), project number A0022A01664.

VI. REFERENCES

- [1] J. P. Whitney and R. J. Wood, "Aeromechanics of passive rotation in flapping flight," *Journal of Fluid Mechanics*, vol. 660, pp. 197-220, 2010.
- [2] D. Ishihara, T. Horie, T. Niho, "An experimental and three-dimensional computational study on the aerodynamic contribution to the passive pitching motion of flapping wings in hovering flies," *Bioinspiration & Biomimetics*, vol. 9, no. 4, 046009, 2014.
- [3] A. R. Ennos, "Inertial and aerodynamic torques on the wings of diptera in flight," *Journal of Experimental Biology*, vol. 142, no. 1, pp. 87-95, 1989.
- [4] R. Åke Norberg, "The pterostigma of insect wings an inertial regulator of wing pitch," *Journal of Comparative Physiology*, vol. 81, no. 1, pp. 9-22, 1972.

- [5] H. V. Phan, H. C. Park, "Wing inertia as a cause of aerodynamically uneconomical flight with high angles of attack in hovering insects," *Journal of Experimental Biology*, vol. 221, no. 19, jeb187369, 2018.
- [6] T. Jakobi, D. Kolomenskiy, T. Ikeda, S. Watkins, A. Fisher, H. Liu, S. Ravi, "Bees with attitude: the effects of directed gusts on flight trajectories," *Biology Open*, vol. 7, bio034074, 2018.
- [7] T. Engels, D. Kolomenskiy, K. Schneider, J. Sesterhenn, "FluSI: A novel parallel simulation tool for flapping insect flight using a Fourier method with volume penalization," *SIAM Journal on Scientific Computing*, vol. 38, no. 5, pp. S3-S24, 2016.
- [8] D. Kolomenskiy, S. Ravi, R. Xu, K. Ueyama, T. Jakobi, T. Engels, T. Nakata, J. Sesterhenn, K. Schneider, R. Onishi, H. Liu, "The dynamics of passive feathering rotation in hovering flight of bumblebees," *Journal of Fluids and Structures*, 2019. <https://doi.org/10.1016/j.jfluidstructs.2019.03.021>
- [9] M. Mitchell, B. Muftakhidinov, T. Winchen et al, "Engauge Digitizer software," [markumitchell.github.io/engauge-digitizer](https://github.com/markumitchell/engauge-digitizer), last accessed: May 7, 2018.
- [10] J. F. V. Vincent, U. G. K. Wegst, "Design and mechanical properties of insect cuticle," *Arthropod Structure and Development*, vol. 33, no. 3, pp. 187-199, 2004.